High-Performance Bioelectronic Circuits Integrated on Biodegradable and Compostable Substrates with Fully Printed Mask-Less Organic Electrochemical Transistors

Roberto Granelli, Ivano Alessandri, Paschalis Gkoupidenis, Irene Vassalini, Zsolt M. Kovács-Vajna, Paul W. M. Blom, and Fabrizio Torricelli*

Organic electrochemical transistors (OECTs) rely on volumetric ion-modulation of the electronic current to provide low-voltage operation, large signal amplification, enhanced sensing capabilities, and seamless integration with biology. The majority of current OECT technologies require multistep photolithographic microfabrication methods on glass or plastic substrates, which do not provide an ideal path toward ultralow cost ubiquitous and sustainable electronics and bioelectronics. At the same time, the development of advanced bioelectronic circuits combining bio-detection, amplification, and local processing functionalities urgently demand for OECT technology platforms with a monolithic integration of high-performance iontronic circuits and sensors. Here, fully printed mask-less OECTs fabricated on thin-film biodegradable and compostable substrates are proposed. The dispensing and capillary printing methods are used for depositing both high- and low-viscosity OECT materials. Fully printed OECT unipolar inverter circuits with a gain normalized to the supply voltage as high as 136.6 V^{-1}, and current-driven sensors for ion detection and real-time monitoring with a sensitivity of up to 506 mV dec^{-1}, are integrated on biodegradable and compostable substrates. These universal building blocks with the top-performance ever reported demonstrate the effectiveness of the proposed approach and can open opportunities for next-generation high-performance sustainable bioelectronics.

1. Introduction

Electrolyte-gated transistors are enabling the development of multifunctional surfaces, intelligent objects, wearable electronics, neuromorphic functions, soft robotics, enhanced medical diagnostics, and seamless bio-interfaces.[1] Among electrolyte-gated transistors, organic electrochemical transistors (OECTs) rely on volumetric ion-modulation of the electronic current to provide low-voltage operation, large signal amplification, and enhanced sensing capabilities.[2] In the past few years, OECTs have demonstrated an ever-increasing capability of contributing to significant advancements in various application fields, including for example chemical,[3,4] physical,[5,6] and biological[7,8] sensors with enhanced sensitivity, low-voltage digital circuits,[9–12] neuromorphic electronics,[13,14] electrophysiological signal recording with high signal-to-noise ratio,[15–18] real-time ion detection for health and environment monitoring,[19–21] in-vitro monitoring and recording of biological functionalities,[22–25] and bio-inspired device functionalities.[26,27] Such a large palette of high-performance applications suggests that OECTs can be used for enhancing the objects' functionalities and augmenting the humans' capabilities, eventually improving our lifestyle and wellbeing. Therefore, OECTs are an emerging key technology for the development of next-generation electronics and bioelectronics.

Although significant effort has been devoted to the optimization of the OECT materials and processes,[28–37] current fabrication approaches mostly rely on conventional photolithographic microfabrication methods, which require the extensive use of solvents for development of the photoresists.[38,39] Unfortunately, these solvents negatively affect the performance of the active polymers used for the OECTs, often demanding for additional multistep parylene vapor coatings and manual peel-out of the sacrificial parylene layers.[4,14,16,19,21,24,25,27,31,35,36,40] This significantly increases the fabrication cost and complexity, limits the easy integration of OECTs with different architectures, and results in a large chemical waste when scaled to high-volume

R. Granelli, I. Alessandri, I. Vassalini, Z. M. Kovács-Vajna, F. Torricelli
Department of Information Engineering
University of Brescia
via Branze 38, Brescia 25123, Italy
E-mail: fabrizio.torricelli@unibs.it
P. Gkoupidenis, P. W. M. Blom
Max Planck Institute for Polymer Research
Ackermannweg 10, 55128 Mainz, Germany

The ORCID identification number(s) for the author(s) of this article can be found under https://doi.org/10.1002/smll.202108077.

ADVANCED
SCIENCE NEWS
www.advancedsciencenews.com

NANO · MICRO
small
www.small-journal.com

production. In addition, chemically resilient substrates are needed, thus limiting the palette of material to glass or specific plastic substrates.

To reduce the fabrication cost and material waste, also simplifying the material and device integration (e.g., the solvents typically used for the photoresist development are not orthogonal to the active polymers), printing techniques offer a very efficient and flexible solution. Along this direction, aerosol jet printed poly(3,4-ethylenedioxythiophene) polystyrene sulfonate (PEDOT:PSS) has been proposed for printing the OECT channel,[41] 3D/ink-jet printed OECTs have been proposed for print-on-demand fabrication of neuromorphic transistors,[42] and screen-printing has been demonstrated a viable method for large-scale integration of OECT-based digital circuits on plastic substrates.[9,10,43] Solution processed OECTs using benign solvents have been recently demonstrated by Reynolds and co-workers.[44] Other hybrid approaches have demonstrated the fabrication of OECTs by thermal evaporation of gold electrodes and ink-jet printing of the polymeric channel on plastic substrates.[7,45]

The rise of electronics and bioelectronics based on plastic transistors is expected to produce high volumes of electronic surfaces and devices that could be easily dispersed in the environment. This is even more critical considering that organic technologies are ideally suited for disposable applications and could contribute to further increasing the plastic pollution. The substrate is the most relevant component in terms of materials used for organic transistor fabrication, as it represents >99.5% of the total material weight.[46–48] Therefore, the development of OECT electronics and bioelectronics on biodegradable or even compostable substrates by adopting low-energy and additive techniques that minimize the material waste, also during the fabrication process, is highly desired. Focusing on biocompatible and biodegradable devices for electrocardiogram recordings, very recently Kim and co-workers demonstrated solid-state electrolyte-based p-type organic transistors.[49] Commercially available P3CPT polymer dissolved in DMSO was spin-coated on PDMS and transferred on a substrate with evaporated gold source and drain electrodes. Although the transfer method can be a viable solution for the fabrication a single device, it is not ideally suited for further device integration. Therefore, direct printing of OECTs on biodegradable or even compostable substrates achieving low-voltage operation, large signal amplification, and high-sensitivity sensing performance is still an open challenge. This would be an ideal approach for the development of enhanced, low-cost, and sustainable electronics and bioelectronics. At the same time, an OECT technology platform with a monolithic integration of high-performance iontronic circuits and sensors is urgently required for the efficient development of advanced bioelectronics.

Here, we combine dispensing and direct writing methods enabling the mask-less fabrication of fully printed OECTs on a 50 μm-thick film of diacetate cellulose, a commercially available biodegradable and compostable substrate. We use the dispensing technique to deposit high-viscosity materials including the conductors, insulator and solid-state electrolyte. Direct writing of low-viscosity PEDOT:PSS with capillary felt tip printing allowed us to deposit and pattern the OECT channel. Fully printed mask-less OECTs are integrated in unipolar inverters and current-driven ion sensors. The inverters show a gain normalized to the supply voltage as high as 136.6 V^{-1}. The current-driven ion sensors show a sensitivity of up to 506 mV dec^{-1}. These top-level performances demonstrate the effectiveness of the proposed approach, providing a viable path for next-generation sustainable bioelectronic circuits and interfaces.

2. Results and Discussion

The schematic structures and the materials of fully printed mask-less OECTs are displayed in **Figure 1**a–c. The OECTs are fabricated on a 50 μm-thick diacetate cellulose film. Diacetate cellulose is a biomass material produced by esterifying hydroxyl groups with acetic acids in cellulose materials derived from nonedible parts of plants, such as wood fibers and cotton. Importantly, diacetate cellulose can be industrially manufactured and is highly biodegradable in soil, compost, and seawater.[50,51] The average degradation time of diacetate cellulose is about 1 year in nature, viz. under environmental conditions. As a comparison, under the same conditions the average degradation time of polyethylene terephthalate (PET) is about 450 years. Moreover, in the case of diacetate cellulose the degradation time reduces to less than 3 months in marine water and less than 2 months in industrial compost.[52]

As a first layer, we deposit by dispensing an ultra-low temperature cure silver conductor used for the nonpolarizable gate electrode, interconnections, and pads. Dispensing technique is simple and allows selective deposition of the materials. The material is loaded into a syringe barrel and mechanically dispensed by an electroactuated piston. The needle diameter and the distance between the needle tip and the substrate define the line dimensions. As an example, Figure 1d shows the dispensing of silver. The barrel is moved automatically by a gantry system according to the pattern designed (Figure S1a-c, Supporting Information). As second layer, we dispensed an insulating pad in correspondence of the channel region, as displayed in Figure S1d (Supporting Information). An ultraviolet (UV) light curable solvent-less dielectric material was used. Moving from one material to the other, e.g. from silver to the insulator, is straightforward and neither cleaning/purging steps are needed nor material waste is produced. Then, a barrel with a felt nib is used for direct writing an aqueous-based PEDOT:PSS solution. Piston actuation is not applied during capillary printing. Importantly, PEDOT:PSS is a commercially available organic mixed ionic electronic conductor (OMIEC)[53] dispersed in a benign solvent (viz. water). Moreover, it has been recently demonstrated that PEDOT:PSS can be easily co-formulated with biodegradable nanocomposites, e.g. montmorillonite (MMT), to obtain a biodegradable polymer MMT/PEDOT:PSS. Eco-biodegradability of the MMT/PEDOT:PSS composites was confirmed by the super-worm's ingestion behaviors and their chemical changes after digestion.[52,54] Printing of PEDOT:PSS is displayed in Figure S1e,f (Supporting Information). We note that the capillary printing and capillary stamping techniques have been demonstrated as alternative solutions for functional ink deposition and patterning.[55–59] For example, Lee and co-workers
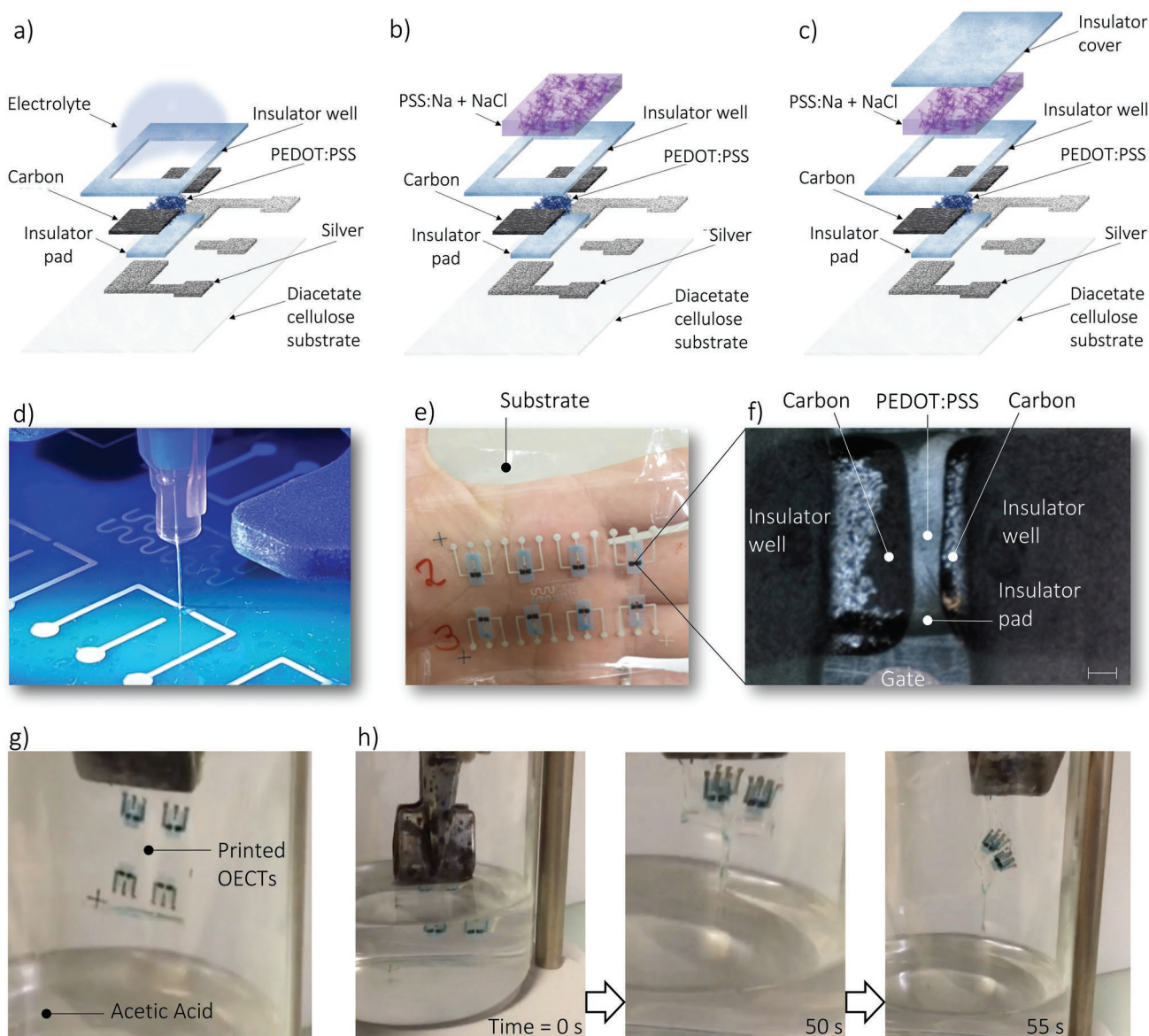
ADVANCED
SCIENCE NEWS
www.advancedsciencenews.com

NANO · MICRO
small
www.small-journal.com

Figure 1. Schematic structures and materials of the fully printed and mask-less organic electrochemical transistors (OECTs) with a) liquid electrolyte, b) solid-state electrolyte, and c) solid-state electrolyte encapsulated by an insulating layer. OECTs are fabricated on diacetate cellulose substrates, silver is used for electrical connections and for the nonpolarizable lateral gate, the insulator pad prevents the penetration of the poly(3,4-ethylenedioxythio-phene) polystyrene sulfonate (PEDOT:PSS) channel into the substrate, source and drain are fabricated with carbon and an insulator well prevents the direct contact between the electrolyte and silver tracks used for the electrical connections. d) Photograph of the dispensing head operated by the gantry system. A silver cartridge is used for printing the gate electrode and the electrical connections. e) Various OECTs printed on a diacetate cellulose substrate. f) The OECT channel is deposited on the top of the insulator pad. Carbon source and drain electrodes are deposited on the top of the PEDOT:PSS channel and covered with the insulator well. Scale bar is 200 µm. g) Fast degradation of diacetate cellulose in acetic acid. Photograph of the printed OECTs on a 50 µm-thick diacetate cellulose. h) Immersion of the printed OECTs in acetic acid at a concentration equal to 90%. Dissolution after 50 and 55 s. Video S1 (Supporting Information) shows the degradation of diacetate cellulose in acetic acid, i.e., an environment-friendly solvent. Cellulose diacetate can be easily dissolved in many common solvents, including esters, cyclic ethers, and ketones. Upon substrate dissolution, the other components of the OECTs can be easily separated and recovered. Video S2 (Supporting Information) shows the real-time, instantaneous dissolution of OECTs printed on diacetate cellulose under acetone flux at room temperature.

introduce capillary pen printing for the fabrication of conventional organic field-effect transistors operating at a supply voltage of 10 V, showing good reproducibility and operational stability.[55–58] Very recently, Hou and co-workers demonstrated scanner-based capillary stamping as a viable approach for upscaling of contact lithography.[59]

As a next step, carbon conductor is dispensed and used for the source and drain electrodes. Carbon electrically connects the PEDOT:PSS channel with the silver tracks. Being ion impermeable and operating as a polarizable material, it prevents redox reactions between the electrolyte and the silver tracks. Because the resistivity of silver is orders of magnitude lower than that of

ADVANCED
SCIENCE NEWS
www.advancedsciencenews.com

NANO · MICRO
small
www.small-journal.com

carbon, silver is used for the interconnections while carbon for source and drain electrodes. A second insulating layer defines a well containing the electrolyte and prevents possible unwanted contacts between the electrolyte and the silver electrical connections. The electrolyte can be an ionic liquid, e.g. a NaCl solution (Figure 1a), or an hydrogel filled with an ionic liquid. Figure 1b shows the schematic structure of an OECT where the liquid electrolyte is replaced with a solid-state hydrogel. We used the PSS:Na polyelectrolyte as hydrogel for internal reservoir. The use of PSS:Na was originally proposed by Malliaras and co-workers for microfabricated ion-selective OECTs with Ag/AgCl pellet as gate electrode[20] and very recently we extended its use to fully integrated OECTs with polarizable gate electrode.[60] With respect to previous works, here the PSS:Na formulation has been optimized for dispensing (see the Experimental Section). To prevent evaporation and/or ambient contamination of the solid-state electrolyte, we developed a third OECT structure (Figure 1c) where an insulating cover layer is used for the encapsulation of the PSS:Na polyelectrolyte. Further details on the OECTs fabrication are provided in the Experimental Section and the various fabrication steps are shown in Figure S2 (Supporting Information). The maximum process temperature is equal to 100 °C, highlighting a low thermal budget for the overall fabrication process. The layout of the various material layers and patterns designed for the fabrication of the OECTs are displayed in Figure S3 (Supporting Information). The details of the geometry and morphology of the printed features are shown in Figure S4 (Supporting Information).

Various OECTs printed on thin-film diacetate cellulose are displayed in Figure 1e. The substrate is fully transparent and can be easily conformed to the body shape. To improve the alignment between the various printed layers and simplify the handling during the fabrication process, the substrates were mechanically pressed to a reusable rigid substrate and easily detached by manual peel-off after the fabrication (Figure S5, Supporting Information). Figure 1f shows the optical image of the PEDOT:PSS channel deposited on the top of the insulator pad. The source and drain carbon electrodes define the channel length and are covered with the insulator well. By design, the width of the carbon electrodes is larger than the width of the PEDOT:PSS layer, thus defining the channel width. The OECT displayed in Figure 1f has channel length and width equal to 200 and 1000 µm, respectively. The lateral Ag gate (partially visible at the bottom of panel 1f) is placed at a distance of about 200 µm from the channel. This minimizes the ion path and, in our technology, prevents shorts between the gate and the carbon electrodes. Figure 1g,h shows a diacetate cellulose foil with printed OECTs dissolved in less than 1 min (Video S1, Supporting Information) when immersed in acetic acid, which is an environment-friendly solvent. Real-time instantaneous dissolution is obtained under acetone flux at room temperature (Video S2, Supporting Information).

Typical transfer ($I_D - V_G$) and output ($I_D - V_D$) characteristics of the fabricated devices are shown in **Figure 2**a,b, respectively. By applying a positive gate voltage (V_G) cations drift into the polymer, reduce the hole concentration, and lower the drain current (I_D). Analogously, when a negative V_G is applied, previously injected cations drift out the polymeric channel while anions drift into the polymer, the hole concentration increases,

and this results in a larger I_D. The measured $I_D - V_G$ of various nominally identical OECTs are shown in Figure 2a (thin lines) and the average $I_D - V_G$ characteristics are highlighted by the thick lines. For the sake of clarity, the various dual-sweep characteristics are displayed in Figure S6 (Supporting Information). The measurements show a very nice reproducibility of the device characteristics in the whole range of gate voltages. This is confirmed by the output characteristics ($I_D - V_D$) of nominally identical OECTs displayed in Figure 2b. Importantly, the $I_D - V_D$ measurements demonstrate that the OECTs show both linear and saturation region of operations and the transition from linear to saturation consistently depends on the applied gate voltage. The average transconductance normalized by the PEDOT:PSS thickness $g_{mn} = g_m/t$ as a function of V_G is shown in Figure 2c. As expected g_{mn} increases by increasing the drain voltage and a maximum value of about 70 S cm^{-1} is obtained when $V_G = 0.1$ and $V_D = -0.2$ V. The low-voltage operation and large transconductance are hallmarks of OECTs inherently due to the nanoscale ionic-electronic interaction into the whole three-dimensional OMIEC channel. Interestingly, the normalized transconductance enables to directly benchmark the proposed OECT technology with the state of art, and we found that the peak g_{mn} of our fully printed OECTs on biodegradable and compostable substrates well compares with that obtained from OECTs fabricated with photolithography on glass and plastic substrates.[4,27,31,37]

Since OECTs are volumetric iontronic devices, the deposited volume of PEDOT:PSS is critical to guarantee good uniformity and reproducibility of the OECT technology. Therefore, to further investigate the variability of the printing process we performed electrochemical impedance spectroscopy (EIS) of various nominally identical printed OECTs. Figure 2d shows the measured (thin light-blue lines) and the average (thick blue line) impedance as a function of frequency, confirming a very consistent deposition of the PEDOT:PSS by using capillary felt tip printing. Then, we measured the electrical characteristics of the OECT architectures with liquid electrolyte (Figure 1a), solid-state PSS:Na ion reservoir (Figure 1b), and solid-state PSS:Na ion reservoir encapsulated with an insulating layer (Figure 1c). The $I_D - V_G$ characteristics are displayed in Figure 2e at various drain voltages. The OECTs are designed with nominally identical geometries. The $I_D - V_G$ curves of the various OECT architectures are almost perfectly overlapped, indicating that ion transport is not limited by the PSS:Na polyelectrolyte and that the deposition of encapsulating layer does not degrade the solid-state electrolyte. These results are confirmed by the EIS measurements displayed in Figure 2f. We note that there is a subtle (almost negligible) increase of the ionic resistance from liquid to solid electrolyte and from solid to solid-covered electrolyte, which is fully consistent with the OECT architectures. As a further confirmation, we evaluate the impact of the various OECT structures by using KCl as electrolyte. Figure S7 (Supporting Information) shows that also in this case the solid-state electrolyte and the covered solid-state electrolyte has a negligible impact on the ionic-electronic characteristics of the OECTs.

In order to investigate the impact of the process temperature on the OECT characteristics, we fabricated fully printed and mask-less OECTs on diacetate cellulose substrates by
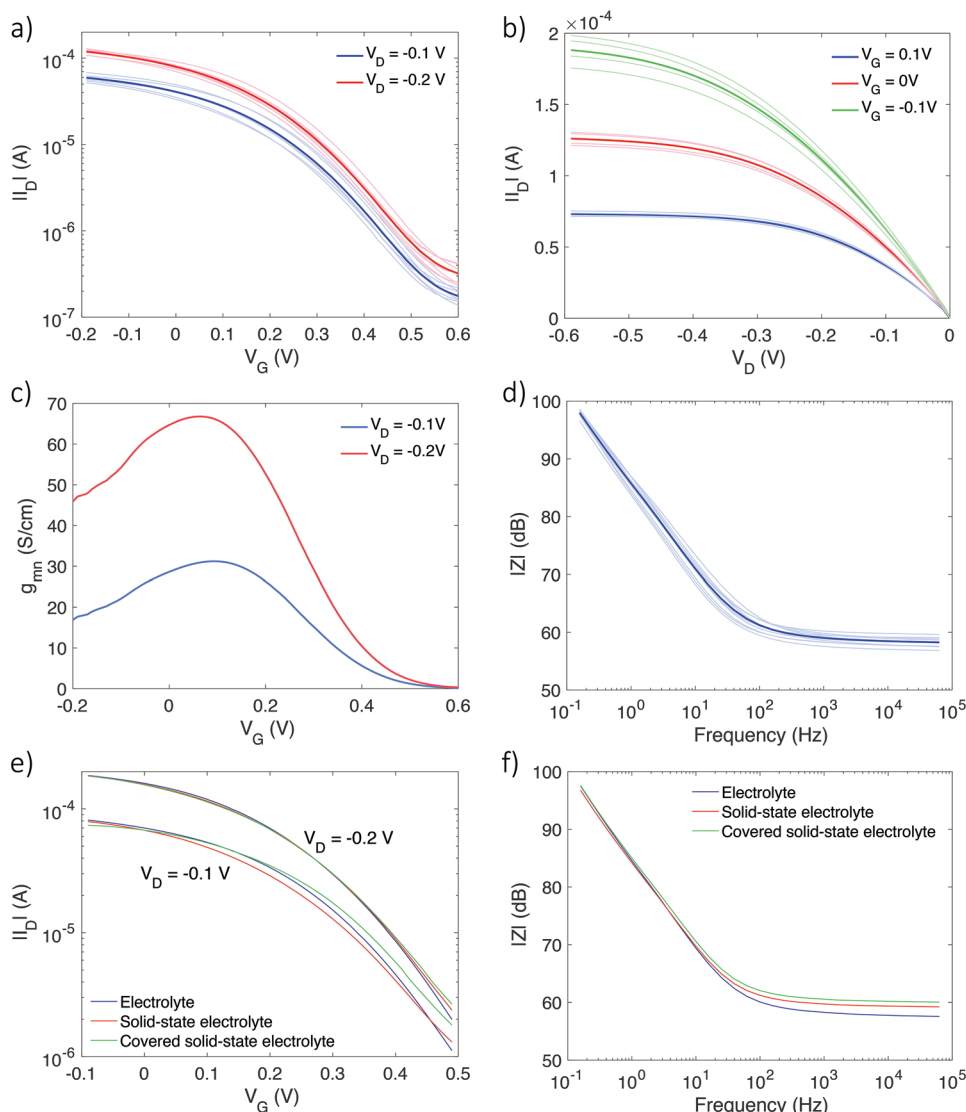
Figure 2. Electrical characteristics of fully printed and mask-less organic electrochemical transistors (OECTs) on diacetate cellulose substrates. a) Measured transfer characteristics ($I_D - V_G$) of eight OECTs at various drain voltages V_D (thin lines). The thick lines are the $I_D - V_G$ obtained as the average of eight OECT characteristics at $V_D = -0.1$ and -0.2 V, respectively. b) Measured output characteristics ($I_D - V_D$) at various gate voltages V_G (thin lines). The thick lines are the average $I_D - V_G$ at various V_G. c) Average transconductance normalized to the poly(3,4-ethylenedioxythiophene) polystyrene sulfonate (PEDOT:PSS) thickness as a function of V_G at various V_D. d) Electrochemical impedance spectroscopy (EIS) measurements of 10 OECTs (thin lines). The thick line is the average impedance. The DC voltage is $V_{DC} = 0$ V and the amplitude of AC voltage is $V_{AC} = 0.01$ V. e) Comparison between the measured $I_D - V_G$ characteristics of OECTs with liquid electrolyte, PSS:Na solid-state electrolyte and PSS:Na solid-state electrolyte encapsulated by the insulator. f) Comparison between the measured EIS of OECTs with liquid electrolyte, PSS:Na solid-state electrolyte and solid-state electrolyte covered by the insulator. $V_{DC} = 0$ V and $V_{AC} = 0.01$ V. In all panels the electrolyte is 10^{-1} M NaCl and the OECT geometries are W = 1000 µm, L = 400 µm, t = 100 nm.

annealing the PEDOT:PSS at a conventional temperature $T_a = 140$ °C and at the reduced annealing temperature $T_a = 100$ °C. Typical $I_D - V_G$ characteristics measured at $V_D = -0.1$ V and $V_D = -0.2$ V are displayed in **Figure 3**a,b, respectively. OECTs fabricated at $T_a = 140$ °C show a lower threshold voltage and a slightly reduced hysteresis with respect to the OECTs fabricated at $T_a = 100$ °C. Figure 3c shows a direct comparison of the $I_D - V_G$ characteristics at various V_D and T_a. To this aim, the transfer characteristics measured at $T_a = 140$ °C are shifted by 0.17 V to the left (more negative V_G). The comparison shows that the $I_D - V_G$ at $T_a = 140$ °C almost perfectly overlap with the

$I_D - V_G$ at $T_a = 100$ °C, and the higher annealing temperature results in a lower threshold voltage of the OECTs. To deep the analysis, the stability as a function of time is investigated in Figure 3d. The full transfer characteristics are consecutively acquired, and the maximum and minimum I_D are displayed as a function of time in the case of PEDOT:PSS OECTs annealed at $T_a = 100$ °C (green lines) and $T_a = 140$ °C (orange lines). The measurements show a very good stability at both the annealing temperatures. The OECTs show an on/off drain current ratio larger than 10^3. We note that the maximum and minimum applied gate voltage is $V_{Gmin} = -0.2$ V and $V_{Gmax} = 0.65$ V,
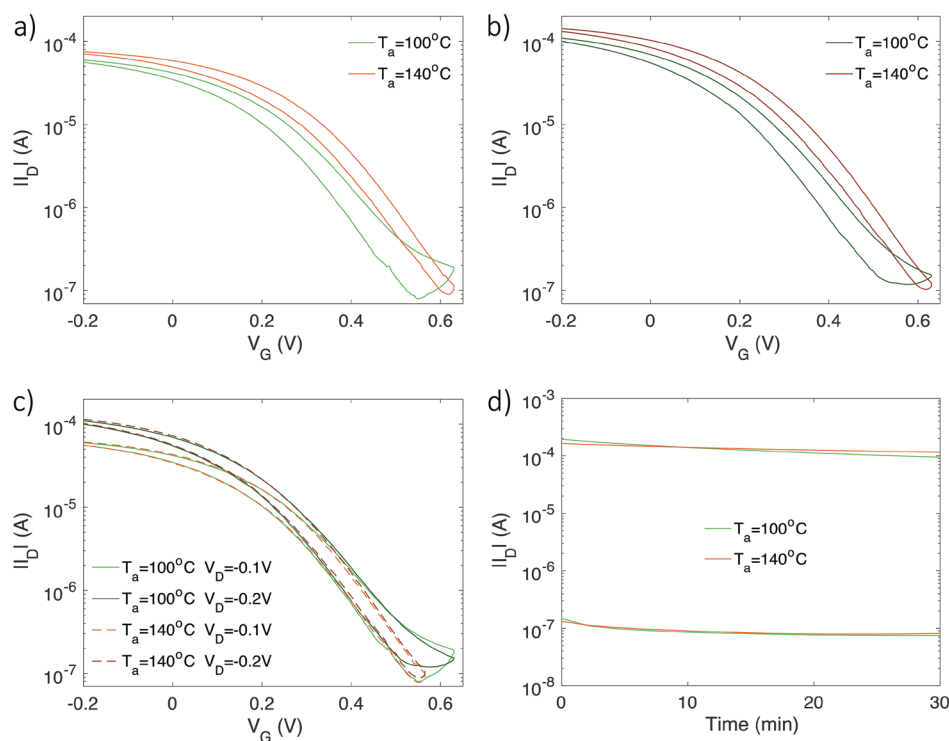
Figure 3. Impact of the process temperature and stability tests of fully printed and mask-less organic electrochemical transistors (OECTs) on diacetate cellulose substrates. Measured transfer characteristics ($I_D - V_G$) at a) $V_D = -0.1$ V and b) $V_D = -0.2$ V. The poly(3,4-ethylenedioxythiophene) polystyrene sulfonate (PEDOT:PSS) annealing temperature is $T_a = 100$ °C (green line) and $T_a = 140$ °C (orange line). c) Comparison of the $I_D - V_G$ characteristics measured at various V_D and T_a. The $I_D - V_G$ measured at $T_a = 140$ °C are shifted by 0.17 V to the left (more negative V_G). d) Stability over time of fully printed and mask-less OECTs on diacetate cellulose substrates with PEDOT:PSS annealed at $T_a = 100$ °C (green line) and $T_a = 140$ °C (orange line). The full $I_D - V_G$ are consecutively acquired for the whole timeframe and the maximum and minimum I_D are displayed. Applied voltages are $V_{Gmin} = -0.2$ V and $V_{Gmax} = 0.65$ V, respectively, and $V_D = -0.2$ V. In all panels the OECT geometries are $W = 1000$ μm, $L = 400$ μm, $t = 100$ nm.

respectively, and $V_D = -0.2$ V, viz. the working conditions of OECTs.

We integrate the OECTs in order to obtain fully printed mask-less unipolar inverter circuits. The inverter is a fundamental building block of any electronic circuit enabling the development of integrated digital and analogue electronics.[61] For example, inverters find application both in digital circuits as logic gates and in analogue circuits as voltage amplifiers. **Figure 4**a shows the schematic structure and the various layers deposited for the fabrication of the inverter circuits. According to the process flow detailed in Figure S2 (Supporting Information), the fabrication is based on dispensing and capillary felt-tip printing. In the inverter circuit the input voltage V_I is applied to the gate of the driver OECT, the supply voltage V_{DD} is applied at its source while the output voltage V_O is collected at the drain, which is also connected to the source of the load OECT. The load OECT is operated in the so-called zero-V_{GS} topology, in order to minimize the power consumption. Importantly, we note that it is possible to independently gate the driver and load OECTs by means of the solid-state electrolyte. An inverter circuit printed on diacetate substrate is shown in Figure 4b. The thin-film biodegradable substrate is mechanically attached to a rigid substrate simplifying the alignment of the various printed layers, and it is easily peeled-off after fabrication (Figure S5d, Supporting Information).

The voltage transfer characteristics ($V_O - V_I$) are displayed in Figure 4c at various supply voltages V_{DD}. When the input

is low (e.g., $V_I = -V_{DD}$) the source-gate voltage V_{SG} applied to the driver OECT is large ($V_{SG} = V_{DD} - V_I$) and, as a result, the output voltage V_{OUT} is close to V_{DD}. By increasing V_I, the pull-up of the driver OECT becomes progressively weaker and a sharp transition of V_O from V_{DD} to $-V_{DD}$ is displayed when V_I is close to V_{DD}. Further increasing V_I reduces V_{SG} of the driver OECT and the pull-down of the load OECT brings V_O close to $-V_{DD}$. As displayed in Figure 4c, an almost rail-to-rail output voltage is obtained and the electrical characteristics scale with V_{DD}. The gain as a function of V_I at various V_{DD} is displayed in Figure 4d. A maximum gain equal to 82 is obtained at a supply voltage $V_{DD} = 0.6$ V. By lowering V_{DD} the gain reduces and at $V_{DD} = 0.5$ V a fairly good value of about 30 is still achieved. The performance of fully printed and mask-less OECT inverters are benchmarked in **Table 1**. In order to directly compare the various OECT inverters, the gain G is normalized to the supply voltage V_{DD}, and we define $G_n = G \ V_{DD}^{-1}$. The comparison shows that our approach enables the fabrication of OECT inverters with an exceptionally high normalized gain (G_n) of up to 136.7 V^{-1}, which is the largest value ever reported. Interestingly, by reducing the supply voltage we surpassed the maximum normalized gain reported in our recent work where a sulfuric acid treatment was necessary for increasing the crystallinity of the polymeric channel (Crys-P) and an external gate was used.[45] We also note that the Crys-P processing method is neither applicable to biodegradable substrates such as diacetate
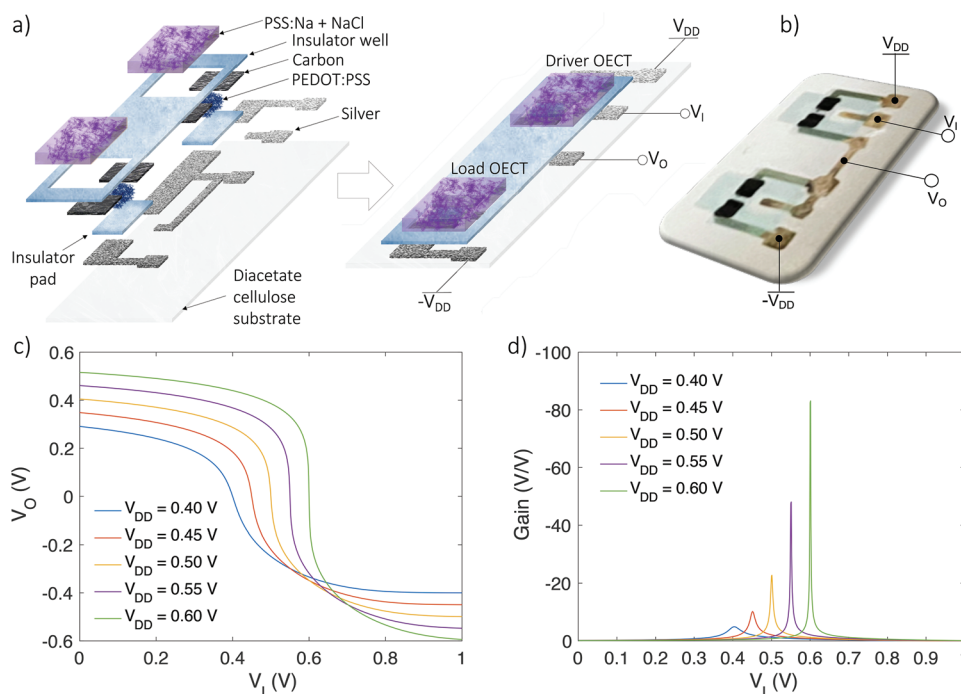
ADVANCED
SCIENCE NEWS
www.advancedsciencenews.com

NANO · MICRO
small
www.small-journal.com

Figure 4. Fully printed and mask-less unipolar organic electrochemical transistor (OECT) inverters integrated on diacetate cellulose substrates. a) Schematic structure and materials. b) Photograph of the fabricated inverter. c) Measured voltage transfer characteristics and d) static gain of an inverter at various supply voltages V_{DD}. The OECT geometries are $W = 1300$ µm, $L = 160$ µm, $t = 100$ nm.

cellulose, nor ideally suited for environmentally sustainable transistor fabrication. Moreover, Table 1 shows that the majority of the state-of-art OECT inverters are fabricated on glass or plastic substrates,[10,11,36,45] and there is only one example of OECT inverters fabricated on chitosan substrate although with a modest maximum $G_n = 12$ V^{-1}.[62] Finally, we observe that in the state-of-art approaches the nonpolarizable gate electrode is not integrated on the OECT substrate and an external quasi-reference bulk electrode is used. In contrast, we integrated all the inverter circuit components on the same biodegradable and compostable substrate by means of mask-less printing methods.

To further assess the broad applicability of the proposed approach, fully printed OECTs were operated in a current-driven configuration.[63,64] The current-driven configuration overcomes the fundamental trade-off between the sensitivity,

operating range, and supply voltage, finding application in bio-electronics, including ion detection and real-time monitoring of cell layers integrity.[24,25] **Figure 5**a shows the schematic circuit configuration and Figure 5b shows a photograph of various nominally identical OECTs printed on flexible foil and connected in a current-driven configuration for high-sensitivity ion detection. To this aim, OECTs gated with a liquid electrolyte are connected in series to a current generator. The input voltage (V_I) is applied to the gate ($V_G = V_I$) while the output voltage (V_O) is measured at the drain ($V_D = V_O$). The bias current I_B is set by the current generator and the topology gives $I_D = I_B$. Typical $V_O - V_I$ characteristics measured by varying the Na$^+$ and K$^+$ concentration in the range 1×10^{-4}–1×10^{0} M are displayed in Figure 5c,d, respectively. By increasing the ion concentration, the electrical characteristics shift to lower input voltages, viz. a lower V_I is required to switch V_O from GND (0 V) to

Table 1. Performance of organic electrochemical transistor (OECT) inverters.

Inverter OECT topology	Substrate	Electrolyte	Gate	Fabrication method	Gain (V/V)	V_{DD} [V]	G_n [V^{-1}]	Ref.
Complementary	Glass	Liquid	External	Photolithography + spin-coating	12	0.6	20.0	[11]
Complementary	Glass	Liquid	External	Photolithography + drop casting	7	0.2	35.0	[62]
Complementary	Chitosan	Liquid	External	Evaporation + shadow mask + drop casting	2.4	0.2	12.0	[62]
Unipolar zero-V_{GS}	Glass	Liquid	External	Photolithography + spin-coating	27	0.8	33.8	[36]
Unipolar zero-V_{GS}	Glass	Liquid	External	Sputtering + shadow mask + spin-coating	107	0.8	133.8	[45]
Unipolar resistive load	PET[a]	Solid-state	Integrated	Screen-printing	30	1.5	20.0	[10]
Unipolar zero-V_{GS}	DA cellulose[b]	Solid-state	Integrated	Dispensing + capillary printing	82	0.6	136.6	This work

The table compares the performance of OECT inverters considering the substrate, electrolyte, gate integration, fabrication process, gain, supply voltage V_{DD}, and normalized gain G_n = Gain V_{DD}^{-1}; [a]Polyethylene terephthalate (PET); [b]Diacetate cellulose (DA cellulose).
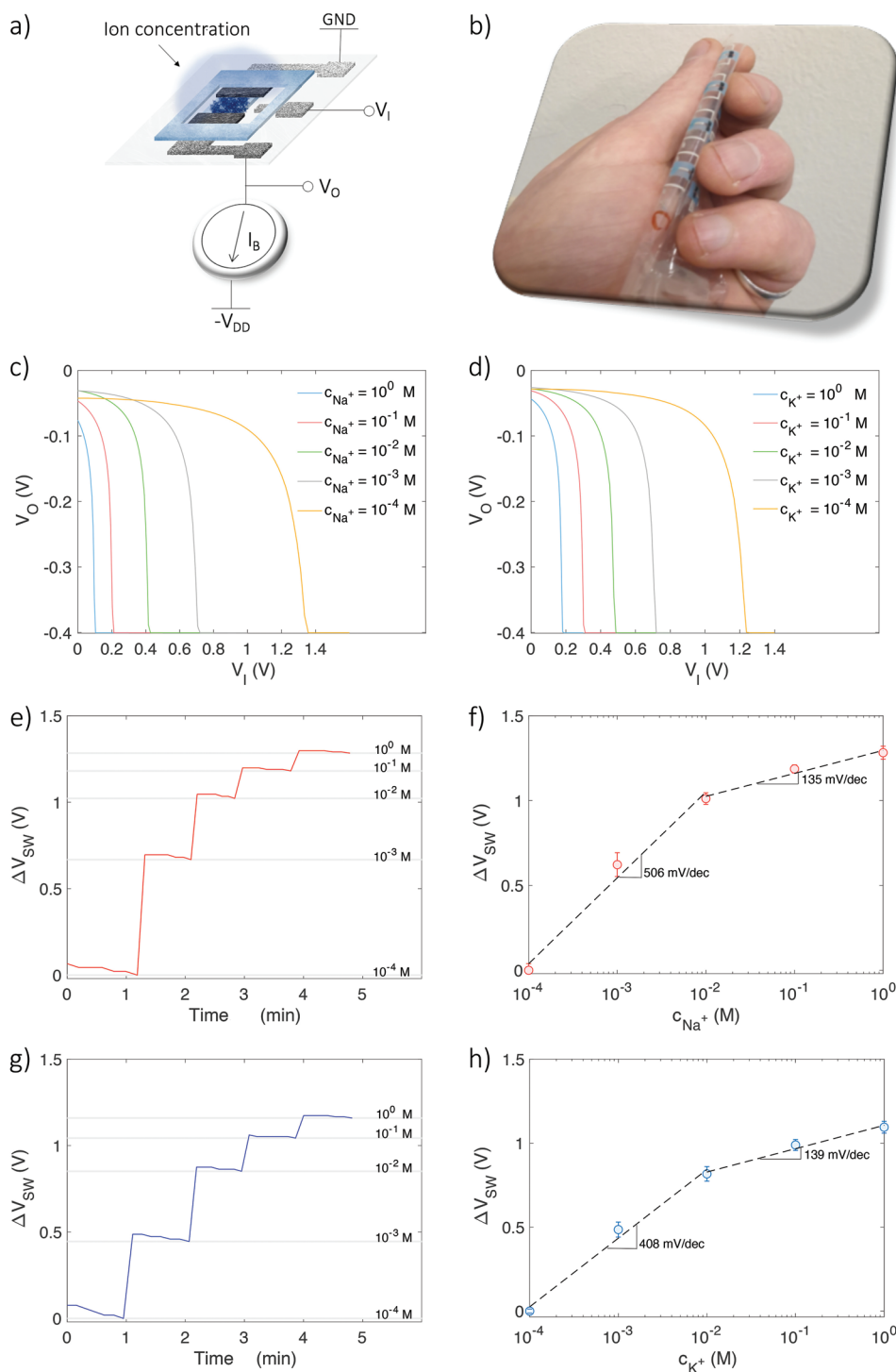
Figure 5. a) Schematic structure of a current-driven organic electrochemical transistor (OECT) configuration operating as ion sensor. b) Photograph of fully printed mask-less current-driven OECT ion sensors integrated on diacetate cellulose substrates. c) Measured characteristics of a current-driven OECT as a function of Na^+ concentration at $V_{DD} = 0.4$ V and $I_B = 100 \times 10^{-6}$ A. d) Measured characteristics of a current-driven OECT as a function of K^+ concentration at $V_{DD} = 0.4$ V and $I_B = 100 \times 10^{-6}$ A. e) Real-time response as a function of Na^+ concentration. The concentration is increased over time from 10^{-4} to 10^0 M. f) Measured (symbols) steady-state ΔV_{SW} as a function of Na^+ concentration. $\Delta V_{SW} = V_{SW}(c_{min}) - V_{SW}(c)$, where $V_{SW}(c_{min})$ and $V_{SW}(c)$ is the measured V_{SW} at the minimum concentration ($c_{min} = 10^{-4}$ M) and at concentration c, respectively. Dashed line is the linear least square fit to the measurements and yields the average sensitivity. g) Real-time response as a function of K^+ concentration. The concentration is increased over time from 10^{-4} to 10^0 M. h) Steady-state ΔV_{SW} as a function of K^+ concentration. In all panels the OECT geometries are $W = 1400$ µm, $L = 450$ µm, $t = 100$ nm.

$-V_{DD}$. This can be explained as follows. The OECT threshold voltage increases, viz. becomes more negative, when the ion concentration increases because of the fixed negative charges into the polyelectrolyte phase, viz PSS phase, of PEDOT:PSS.[45] We defined the switching voltage V_{SW} as the input voltage V_I required to obtain $V_O = -V_{DD}$. The real-time monitoring of the ion concentration is displayed in Figure 5e. A fast significant variation of the switching voltage ΔV_{SW} is measured by varying the ion concentration. Figure S8 (Supporting Information) shows the measured characteristics when the Na$^+$ concentration is decreased from 10^0 to 10^{-4} M (Figure S8a, Supporting Information), then increased from 10^{-4} to 10^0 M (Figure S8b, Supporting Information) and finally decreased again to 10^{-4} M (Figure S8c, Supporting Information). The recorded V_{SW} as a function of time is displayed in Figure S9 (Supporting Information). The steady-state response as a function of Na$^+$ concentration is shown in Figure 5f. Symbols are the average value and error bars are the standard deviation calculated considering the decreasing, increasing, and decreasing loops of the ion concentration. The very small error bars quantitively demonstrate that the fully printed mask-less current-driven OECT sensors show an excellent reversibility and stability. The least square linear approximation of the measured ΔV_{SW} as a function of c_{Na+} (Figure 5f, dashed lines) provides an average sensitivity equal to $S_V = 506$ mV dec^{-1} when the ion concentration range is $1 \times 10^{-4} - 1 \times 10^{-2}$ M that reduces to 135 mV dec^{-1} when the ion concentration range is $1 \times 10^{-2} - 1 \times 10^0$ M.

To further corroborate these results, Figure 5g shows the real-time monitoring of K$^+$ concentration. In this case K$^+$ concentration was first increased from 10^{-4} to 10^0 M, then decreased from 10^0 to 10^{-4} M and then increased again from 10^{-4} to 10^0 M. The various $V_O - V_I$ and $\Delta V_{SW} - c_{K+}$ measurements are displayed in Figures S10 and S11 (Supporting Information), respectively. The steady-state response as a function of K$^+$ concentration is shown in Figure 5h. Symbols are the average value and error bars are the standard deviation calculated considering the increasing, decreasing, and increasing loops of the K$^+$ concentration. According to the detection of the Na$^+$ concentration, also in the case of K$^+$ ion detection the very small error bars confirm the reversibility of the ion sensor. The least square linear approximation of the $\Delta V_{SW} - c_{K+}$ characteristic (Figure 5h, dashed lines) provides an average sensitivity equal to $S_V = 408$ mV dec^{-1} in the ion concentration range $1 \times 10^{-4} - 1 \times 10^{-2}$ M and 139 mV dec^{-1} in the ion concentration range $1 \times 10^{-2} - 1 \times 10^0$ M. This confirms that the voltage sensitivity increases by decreasing the ion concentration range, which is an important feature to detect small variations of ion concentrations, viz. $\Delta c_{min} = [10^\wedge(\Delta V_{SW,min} \ S_V^{-1}) -1] \ c_{max}$, where c_{max} is the maximum concentration in the operative range. To be conservative, we can assume that $\Delta V_{SW,min} = 1\% \ V_{DD}$, viz. in our case 4×10^{-3} V, and we obtain $\Delta c_{min(Na+)} = 1.8 \times 10^{-5}$ M when $c_{max} = 10^{-3}$ M and $\Delta c_{min(Na+)} = 7.1 \times 10^{-2}$ M when $c_{max} = 10^0$ M. Analogous results are obtained in the case of K$^+$ ion detection. Therefore, we found that we are able to detect small variations of ion concentration when the maximum ion concentration to be measured is reduced and we obtained an average $\Delta c_{min}/c_{max} \cong 4.5\%$ over the whole accessed range (viz. 10^{-4}–10^0 M). This feature enables to address a broad range of ion sensing applications.[65,66]

The performance of current-driven OECTs printed on biodegradable and compostable substrate are benchmarked with several ion-sensitive transistor technologies in **Table 2** showing that our printed OECT ion sensors outperforms silicon,[67] metal-oxide,[68] carbon nanotubes,[69] graphene,[70] electrolyte-gated organic field-effect transistors,[71] and OECTs.[20,21,63,72–74] Moreover, we note that the majority of state-of-art

Table 2. Performance of transistor-based sensors for high-sensitivity ion detection and monitoring.

Configuration	Channel	Substrate	Technology	Ion	Range [dec]	S_I [µA dec^{-1}]	S_V [mV dec^{-1}]	Ref.
ISFET	Silicon	Silicon	CMOS fabrication process	Na$^+$, K$^+$	4	–	31.6	[67]
ISFET	CNT	Silicon	Photolithography and dropping	Na$^+$	3	–	71.7	[69]
Dual-gate TFT	a-IGZO	Silicon	Sputtering and photolithography	H$^+$	5	–	16.0	[68]
FET	Graphene	Silicon	Evaporation, etching, and transfer	K$^+$	4	–	64.0	[70]
EGOFET	P3HT	PET	Photolithography and spin coating	Na$^+$	5	179	124.0	[71]
OECT	PEDOT:PSS	Glass	Photolithography, CVD, and spin coating	K$^+$	5	72	120.0	[72]
OECT	PEDOT:PSS	Glass	Photolithography and spin coating	Na$^+$	4	–	135.0	[63]
Membrane-less OECT	PEDOT:PSS	Glass	Photolithography, CVD, and spin coating	Na$^+$, K$^+$	5	25	–	[21]
Integrated IS-OECT	PEDOT:PSS	Polyimide	Photolithography, CVD, and spin coating	Na$^+$, K$^+$	5	–	83.0	[73]
Integrated IS-OECT	PEDOT:PSS	Glass	Photolithography, CVD, and spin coating	Na$^+$, K$^+$	5	98	85.0	[20]
Integrated IS-OECT	PEDOT:PSS	Glass	Photolithography, CVD, and spin coating	Na$^+$, K$^+$	4	35	–	[60]
Current-driven OECT	PEDOT:PSS	Glass	Photolithography and spin coating	Na$^+$	4	–	243.0	[63]
Current-driven OECT	PEDOT:PSS:IL	Silicon	Evaporation and spin coating	Na$^+$	2	–	214.3	[74]
Current-driven OECT	PEDOT:PSS	DA cellulose	Dispensing and capillary printing	Na$^+$	4	–	506.0	This work
Current-driven OECT	PEDOT:PSS	DA cellulose	Dispensing and capillary printing	K$^+$	4	–	408.0	This work

The table compares the performance of several transistor-based ion sensors considering the channel material, the substrate, the fabrication technology, ions, ion concentration range, current (S_I) and voltage (S_V) sensitivity.

approaches[20,21,60,67–70,72,74] use silicon or glass substrates and photolithography that, because of wet processing and chemical etching, is not ideally suited for biodegradable and compostable substrates.

3. Conclusion

In conclusion, we have proposed mask-less fully printing fabrication of high-performance OECT devices, inverter circuits and ion sensors on thin-film biodegradable and compostable substrates. We used dispensing and capillary printing methods for depositing both high- and low-viscosity materials required for the OECT fabrication and integration. The dispensing technique has been ideally suited for the selective deposition of high-viscosity materials including conductors, insulator, and solid-state electrolyte while capillary printing has enabled the simple and reliable direct writing of low-viscosity PEDOT:PSS channel. We note that by increasing the viscosity[75] of commercially available PEDOT:PSS it could be possible to fabricate the OECTs using only the dispensing method. Good reproducibility of the various OECT architectures suitable for both electronic and bioelectronic applications has been demonstrated. The proposed approach, based only on printing techniques, enables the deposition, patterning, and integration of the various structures without any material and solvent waste, also providing the benefits of rapid prototyping and easy upscaling at low costs. Fully printed mask-less OECTs have been integrated in unipolar inverter circuits with a gain normalized to the supply voltage as high as 136.6 V^{-1}. Moreover, printed current-driven OECT sensors provided ion detection and real-time monitoring with a sensitivity of up to 506 mV dec^{-1}. These top-performance universal building blocks offer relevant possibilities for next-generation integrated bioelectronic circuits. Prospectively, the proposed approach can be extended to any iontronic transistor technology, opening new opportunities for the widespread adoption of low-cost, sustainable, and high-performance printing technologies in several fields including disposable devices for medical diagnostics, food and environmental monitoring,[76] on-body sensor systems (e.g., smart patches and bandage),[77] bio-robotics, wearables, and neuromorphic biointerfaces.[78]

4. Experimental Section

Materials: PEDOT:PSS (Clevios PH500) was purchased from Heraeus and filtered with a 0.22 µm cellulose filter. Ethylene glycol (EG), 4-dodecylbenzenesulfonic acid (DBSA), (3-glycidyloxypropyl) trimethoxysilane (GOPS), poly(sodium-4-styrene sulfonate) (PSS:Na) (molecular weight = 1 000 000), sodium chloride (NaCl), and potassium chloride (KCl) were acquired from Sigma-Aldrich and used without further purification. Silver ink (PE828), carbon ink (7102), and dielectric ink (5018) were acquired from Dupont. 50 µm-thick diacetate cellulose substrates were supplied by Pütz-Folien. 5cc barrels (7050LL1DPK) and 30G needles (TE730050PK) were acquired from Techcon.

Polymer Blend Preparation: PEDOT:PSS was mixed with 5 vol% EG and 1 vol% GOPS and vigorously mixed for 5 min The PSS:Na gel was obtained as follows. An amount of 120 mg of PSS:Na was mixed with 500 µL of deionized water, 100 µL of HCl 1 ᴍ, 25 µL of DBSA, and 100 µL of GOPS. The solution was stirred 60 min at room temperature and deposited immediately after the preparation.

Fabrication of OECTs and Ion Sensors: All the devices, circuits, and sensors were fabricated on diacetate cellulose substrate according to the following procedure. As a first step, the substrate was treated with UV ozone cleaner for 5 min. Then, the gate and interconnections were printed by dispensing the silver conductor. The insulator pad was printed by dispensing an UV-curable dielectric. After baking 15 min at 100 °C under UV-C light, PEDOT:PSS was deposited by felt-tip capillary printing and baked for 15 min at 100 °C. As a next step, source/drain carbon electrodes were dispensed and baked for 10 min at 100 °C. A well was printed by dispensing the dielectric cured for 15 min under UV-A light.

Fabrication of Solid-State OECTs and Inverter Circuits: Solid-state OECTs and inverters were obtained by following the fabrication process described above for OECTs and on the top of the PEDOT:PSS the ion-conducting polymer PSS:Na was dispensed and baked 15 min at 100 °C. Then, PSS:Na was hydrated with 1 µL of NaCl and in the case of encapsulated OECTs the insulating ink was dispensed and cured for 30 min with UV-A light. All the annealing steps were performed on a hot-plate. All the dispensing steps were performed using 5cc barrels filled with 2cc of the various inks.

Printing Parameters: For all the material dispensed there are four printing parameters. Specifically, the dispense height (DH) is the distance from the tip of the nozzle to the substrate while dispensing, the federate (FR) is the horizontal (x–y) speed while dispensing, the anti-stringing distance (ASD) is the maximum distance the dispenser will retrace to separate the nozzle from the dispensed ink, and the kick (KK) is the distance traveled by the dispenser's piston to initiate dispensing. Here, we provide the parameters of each material dispensed. Silver ink: DH = 70 µm, FR = 80 mm min^{-1}, ASD = 300 µm, and KK = 100 µm. Carbon ink: DH = 150 µm, FR = 100 mm min^{-1}, ASD = 500 µm, and KK = 80 µm. Insulator ink: DH = 160 µm, FR = 80 mm min^{-1}, ASD = 100 µm, and KK = 80 µm. PSS:Na ink: DH = 200 µm, FR = 80 mm min^{-1}, ASD = 100 µm, and KK = 100 µm. The capillary printed PEDOT:PSS ink was deposited with the following parameters: DH = 0 µm, FR = 50 mm min^{-1}, ASD = 100 µm, and KK = 50 µm.

Electrical Characterization: The DC electrical characteristics were measured with source measure unit (SMU). The applied gate or drain voltages were varied with a scan rate 50 × 10^{-3} V s^{-1}. The EIS were performed in a two-electrode configuration, where the nonpolarizable gate electrode was used as reference electrode. The source and drain electrodes were shorted together, and the OECT channel was used as working electrode.

Supporting Information

Supporting Information is available from the Wiley Online Library or from the author.

Acknowledgements

Conflict of Interest

The authors declare no conflict of interest.

Data Availability Statement

The data that support the findings of this study are available from the corresponding author upon reasonable request.

[1] F. Torricelli, D. Z. Adrahtas, Z. Bao, M. Berggren, F. Biscarini, A. Bonfiglio, C. A. Bortolotti, C. D. Frisbie, E. Macchia, G. G. Malliaras, I. McCulloch, M. Moser, T.-Q. Nguyen, R. M. Owens, A. Salleo, A. Spanu, L. Torsi, *Nat. Rev. Methods Primers* **2021**, *1*, 66.

[2] J. Rivnay, S. Inal, A. Salleo, R. M. Owens, M. Berggren, G. G. Malliaras, *Nat. Rev. Mater.* **2018**, *3*, 17086.

[3] L. M. M. Ferro, L. Merces, D. H. S. de Camargo, C. C. Bof Bufon, *Adv. Mater.* **2021**, *33*, 2101518.

[4] S. T. M. Tan, A. Giovannitti, A. Melianas, M. Moser, B. L. Cotts, D. Singh, I. McCulloch, A. Salleo, *Adv. Funct. Mater.* **2021**, *31*, 2010868.

[5] X. Wang, X. Meng, Y. Zhu, H. Ling, Y. Chen, Z. Li, M. C. Hartel, M. R. Dokmeci, S. Zhang, A. Khademhosseini, *IEEE Electron Device Lett.* **2021**, *42*, 46.

[6] Y. Yan, X. Wu, Q. Chen, Y. Liu, H. Chen, T. Guo, *ACS Appl. Mater. Interfaces* **2019**, *11*, 20214.

[7] E. Macchia, P. Romele, K. Manoli, M. Ghittorelli, M. Magliulo, Z. M. Kovács-Vajna, F. Torricelli, L. Torsi, *Flexible Printed Electron.* **2018**, *3*, 034002.

[8] K. Guo, S. Wustoni, A. Koklu, E. Díaz-Galicia, M. Moser, A. Hama, A. A. Alqahtani, A. N. Ahmad, F. S. Alhamlan, M. Shuaib, A. Pain, I. McCulloch, S. T. Arold, R. Grünberg, S. Inal, *Nat. Biomed. Eng.* **2021**, *5*, 666.

[9] P. C. Hutter, T. Rothländer, G. Scheipl, B. Stadlober, *IEEE Trans. Electron Devices* **2015**, *62*, 4231.

[10] P. Andersson Ersman, R. Lassnig, J. Strandberg, D. Tu, V. Keshmiri, R. Forchheimer, S. Fabiano, G. Gustafsson, M. Berggren, *Nat. Commun.* **2019**, *10*, 5053.

[11] H. Sun, M. Vagin, S. Wang, X. Crispin, R. Forchheimer, M. Berggren, S. Fabiano, *Adv. Mater.* **2018**, *30*, 1704916.

[12] J. J. Samuel, A. Garudapalli, A. A. Mohapatra, C. Gangadharappa, S. Patil, N. P. B. Aetukuri, *Adv. Funct. Mater.* **2021**, *31*, 2102903.

[13] I. Krauhausen, P. Gkoupidenis, A. Melianas, S. T. Keene, K. Lieberth, H. Ledanseur, R. Sheelamanthula, D. Koutsouras, F. Torricelli, I. Mcculloch, P. W. M. Blom, A. Salleo, Y. van de Burgt, A. Giovannitti **2021**, *7*, eabl5068.

[14] X. Ji, B. D. Paulsen, G. K. K. Chik, R. Wu, Y. Yin, P. K. L. Chan, J. Rivnay, *Nat. Commun.* **2021**, *12*, 2480.

[15] D. M. Yuanying Liang, M. Ernst, F. Brings, D. Kireev, V. Maybeck, A. Offenhäusser, *Adv. Healthcare Mater.* **2018**, *7*, 1800304.

[16] C. Cea, G. D. Spyropoulos, P. Jastrzebska-Perfect, J. J. Ferrero, J. N. Gelinas, D. Khodagholy, *Nat. Mater.* **2020**, *19*, 679.

[17] C. G. Bischak, L. Q. Flagg, D. S. Ginger, *Adv. Mater.* **2020**, *32*, 2002610.

[18] J. E. Tyrrell, M. G. Boutelle, A. J. Campbell, *Adv. Funct. Mater.* **2021**, *31*, 2007086.

[19] P. Romele, P. Gkoupidenis, D. A. Koutsouras, K. Lieberth, Z. M. Kovács-Vajna, P. W. M. Blom, F. Torricelli, *Nat. Commun.* **2020**, *11*, 3743.

[20] S. Han, S. Yamamoto, A. G. Polyravas, G. G. Malliaras, *Adv. Mater.* **2020**, *32*, 2004790.

[21] S. Wustoni, C. Combe, D. Ohayon, M. H. Akhtar, I. McCulloch, S. Inal, *Adv. Funct. Mater.* **2019**, *29*, 1904403.

[22] C. Yao, C. Xie, P. Lin, F. Yan, P. Huang, I.-M. Hsing, *Adv. Mater.* **2013**, *25*, 6575.

[23] R. M. Owens, S. Daniel, A. M. Pappa, H. Y. Liu, W. Traberg-Christensen, Q. Thiburce, A. Savva, A. Pavia, A. Salleo, *ACS Nano* **2020**, *14*, 12538.

[24] L. V. Lingstedt, M. Ghittorelli, M. Brückner, J. Reinholz, N. I. Crăciun, F. Torricelli, V. Mailänder, P. Gkoupidenis, P. W. M. Blom, *Adv. Healthcare Mater.* **2019**, *8*, 1900128.

[25] K. Lieberth, M. Brückner, F. Torricelli, V. Mailänder, P. Gkoupidenis, P. W. M. Blom, *Adv. Mater. Technol.* **2021**, *6*, 2000940.

[26] S. J. Kim, J. S. Jeong, H. W. Jang, H. Yi, H. Yang, H. Ju, J. A. Lim, *Adv. Mater.* **2021**, *33*, 2100475.

[27] D. A. Koutsouras, M. H. Amiri, P. W. M. Blom, F. Torricelli, K. Asadi, P. Gkoupidenis, *Adv. Funct. Mater.* **2021**, *31*, 2011013.

[28] L. Huang, Z. Wang, J. Chen, B. Wang, Y. Chen, W. Huang, L. Chi, T. J. Marks, A. Facchetti, *Adv. Mater.* **2021**, *33*, 2007041.

[29] T. Nicolini, J. Surgailis, A. Savva, A. D. Scaccabarozzi, R. Nakar, D. Thuau, G. Wantz, L. J. Richter, O. Dautel, G. Hadziioannou, N. Stingelin, *Adv. Mater.* **2021**, *33*, 2005723.

[30] A. T. Lill, D. X. Cao, M. Schrock, J. Vollbrecht, J. Huang, T. Nguyen-Dang, V. V. Brus, B. Yurash, D. Leifert, G. C. Bazan, T. Q. Nguyen, *Adv. Mater.* **2020**, *32*, 1908120.

[31] S. T. Keene, T. P. A. van der Pol, D. Zakhidov, C. H. L. Weijtens, R. A. J. Janssen, A. Salleo, Y. van de Burgt, *Adv. Mater.* **2020**, *32*, 2000270.

[32] A. F. Paterson, A. Savva, S. Wustoni, L. Tsetseris, B. D. Paulsen, H. Faber, A. H. Emwas, X. Chen, G. Nikiforidis, T. C. Hidalgo, M. Moser, I. P. Maria, J. Rivnay, I. McCulloch, T. D. Anthopoulos, S. Inal, *Nat. Commun.* **2020**, *11*, 3004.

[33] A. Savva, R. Hallani, C. Cendra, J. Surgailis, T. C. Hidalgo, S. Wustoni, R. Sheelamanthula, X. Chen, M. Kirkus, A. Giovannitti, A. Salleo, I. McCulloch, S. Inal, *Adv. Funct. Mater.* **2020**, *30*, 1907657.

[34] L. V. Lingstedt, M. Ghittorelli, H. Lu, D. A. Koutsouras, T. Marszalek, F. Torricelli, N. I. Crăciun, P. Gkoupidenis, P. W. M. Blom, *Adv. Electron. Mater.* **2019**, *5*, 1800804.

[35] G. D. Spyropoulos, J. N. Gelinas, D. Khodagholy, *Sci. Adv.* **2019**, *5*, eaau7378.

[36] S. E. Doris, A. Pierre, R. A. Street, *Adv. Mater.* **2018**, *30*, 1706757.

[37] S.-M. Kim, C.-H. Kim, Y. Kim, N. Kim, W.-J. Lee, E.-H. Lee, D. Kim, S. Park, K. Lee, J. Rivnay, M.-H. Yoon, *Nat. Commun.* **2018**, *9*, 3858.

[38] B. A. A. Zakhidov, J. Lee, H. H. Fong, J. A. Defranco, M. Chatzichristidi, P. G. Taylor, C. K. Ober, G. Malliaras, *Adv. Mater.* **2008**, *20*, 3481.

[39] B. P. G. Taylor, J. Lee, A. A. Zakhidov, M. Chatzichristidi, H. H. Fong, J. A. Defranco, G. Malliaras, C. K. Ober, **2009**, *1501*, 2314.

[40] A. Melianas, T. J. Quill, G. LeCroy, Y. Tuchman, H. V. Loo, S. T. Keene, A. Giovannitti, H. R. Lee, I. P. Maria, I. McCulloch, A. Salleo, *Sci. Adv.* **2020**, *6*, eabb2958.

[41] G. Tarabella, D. Vurro, S. Lai, P. D'Angelo, L. Ascari, S. Iannotta, *Flexible Printed Electron.* **2020**, *5*, 014005.

[42] T. N. Mangoma, S. Yamamoto, G. G. Malliaras, R. Daly, *Adv. Mater. Technol.* **2022**, *7*, 2000798.

[43] M. Zabihipour, R. Lassnig, J. Strandberg, M. Berggren, S. Fabiano, I. Engquist, P. Andersson Ersman, *npj Flex. Electron.* **2020**, *4*, 15.

[44] B. Schmatz, A. W. Lang, J. R. Reynolds, *Adv. Funct. Mater.* **2019**, *29*, 1905266.

[45] P. Romele, M. Ghittorelli, Z. M. Kovács-Vajna, F. Torricelli, *Nat. Commun.* **2019**, *10*, 3044.

[46] F. Torricelli, I. Alessandri, E. Macchia, I. Vassalini, M. Maddaloni, L. Torsi, **2021**, *7*, 2100445.

[47] W. Li, Q. Liu, Y. Zhang, C. Li, Z. He, W. C. H. Choy, P. J. Low, P. Sonar, A. K. K. Kyaw, *Adv. Mater.* **2020**, *32*, 2001591.

[48] Y. W. Lim, J. Jin, B. S. Bae, *Adv. Mater.* **2020**, *32*, 1907143.

ADVANCED
SCIENCE NEWS

www.advancedsciencenews.com

NANO · MICRO
small

www.small-journal.com

[49] Y. J. Jo, H. Kim, J. Ok, Y. J. Shin, J. H. Shin, T. H. Kim, Y. Jung, T. I. Kim, *Adv. Funct. Mater.* **2020**, *30*, 1909707.

[50] E. M. N. Polman, G. J. M. Gruter, J. R. Parsons, A. Tietema, *Sci. Total Environ.* **2021**, *753*, 141953.

[51] J. Puls, S. A. Wilson, D. Hölter, *J. Polym. Environ.* **2011**, *19*, 152.

[52] S. Lee, Y. Hong, B. S. Shim, *Adv. Sustainable Syst.* **2022**, *6*, 2100056.

[53] B. D. Paulsen, K. Tybrandt, E. Stavrinidou, J. Rivnay, *Nat. Mater.* **2020**, *19*, 13.

[54] V. R. Feig, H. Tran, Z. Bao, *ACS Cent. Sci.* **2018**, *4*, 337.

[55] B. Kang, H. Min, U. Seo, J. Lee, N. Park, K. Cho, H. S. Lee, *Adv. Mater.* **2013**, *25*, 4117.

[56] W. H. Lee, H. Min, N. Park, J. Lee, E. Seo, B. Kang, K. Cho, H. S. Lee, *ACS Appl. Mater. Interfaces* **2013**, *5*, 7838.

[57] B. Kang, N. Park, H. Min, J. Lee, H. Jeong, S. Baek, K. Cho, H. S. Lee, *Adv. Electron. Mater.* **2015**, *1*, 1500301.

[58] Z. Li, H. Liu, C. Ouyang, W. Hong Wee, X. Cui, T. Jian Lu, B. Pingguan-Murphy, F. Li, F. Xu, *Adv. Funct. Mater.* **2016**, *26*, 165.

[59] P. Hou, R. Kumar, B. Oberleiter, R. Kohns, D. Enke, U. Beginn, H. Fuchs, M. Hirtz, M. Steinhart, *Adv. Funct. Mater.* **2020**, *30*, 2001531.

[60] D. A. Koutsouras, K. Lieberth, F. Torricelli, P. Gkoupidenis, P. W. M. Blom, *Adv. Mater. Technol.* **2021**, *6*, 2100591.

[61] T. Leydecker, Z. M. Wang, F. Torricelli, E. Orgiu, *Chem. Soc. Rev.* **2020**, *49*, 7627.

[62] L. Travaglini, A. P. Micolich, C. Cazorla, E. Zeglio, A. Lauto, D. Mawad, *Adv. Funct. Mater.* **2021**, *31*, 2007205.

[63] M. Ghittorelli, L. Lingstedt, P. Romele, N. I. Crˇciun, Z. M. Kovács-Vajna, P. W. M. Blom, F. Torricelli, *Nat. Commun.* **2018**, *9*, 1441.

[64] K. Lieberth, P. Romele, F. Torricelli, D. A. Koutsouras, M. Brückner, V. Mailänder, P. Gkoupidenis, P. W. M. Blom, *Adv. Healthcare Syst.* **2021**, *10*, 2100845.

[65] O. Cozzolino, M. Marchese, F. Trovato, E. Pracucci, G. M. Ratto, M. G. Buzzi, F. Sicca, F. M. Santorelli, *Front. Neurol.* **2018**, *9*, 19.

[66] J. V. Raimondo, R. J. Burman, A. A. Katz, C. J. Akerman, *Front. Cell. Neurosci.* **2015**, *9*, 419.

[67] J. Zhang, M. Rupakula, F. Bellando, E. Garcia Cordero, J. Longo, F. Wildhaber, G. Herment, H. Guérin, A. M. Ionescu, *ACS Sens.* **2019**, *4*, 2039.

[68] N. Kumar, J. Kumar, S. Panda, *IEEE Electron Device Lett.* **2016**, *37*, 500.

[69] S. C. Park, H. J. Jeong, M. Heo, J. H. Shin, J. H. Ahn, *ACS Appl. Electron. Mater.* **2021**, *3*, 2580.

[70] H. Li, Y. Zhu, M. S. Islam, M. A. Rahman, K. B. Walsh, G. Koley, *Sens. Actuators, B* **2017**, *253*, 759.

[71] K. Schmoltner, J. Kofler, A. Klug, E. J. W. List-Kratochvil, *Adv. Mater.* **2013**, *25*, 6895.

[72] M. Sessolo, J. Rivnay, E. Bandiello, G. G. Malliaras, H. J. Bolink, *Adv. Mater.* **2014**, *26*, 4803.

[73] A. Pierre, S. E. Doris, R. Lujan, R. A. Street, *Adv. Mater. Technol.* **2019**, *4*, 1800577.

[74] X. Wu, A. Surendran, J. Ko, O. Filonik, E. M. Herzig, P. Müller-Buschbaum, W. L. Leong, *Adv. Mater.* **2019**, *31*, 1805544.

[75] S. D. Hoath, S. Jung, W. Hsiao, I. M. Hutchings, *Org. Electron.* **2012**, *13*, 3259.

[76] C. Dincer, R. Bruch, E. Costa-Rama, M. T. Fernández-Abedul, A. Merkoçi, A. Manz, G. A. Urban, F. Güder, *Adv. Mater.* **2019**, *31*, 1806739.

[77] H. Jeong, J. A. Rogers, S. Xu, *Sci. Adv.* **2020**, *6*, eabd4794.

[78] I. Krauhausen, D. A. Koutsouras, A. Melianas, S. T. Keene, K. Lieberth, H. Ledanseur, R. Sheelamanthula, A. Giovannitti, F. Torricelli, I. McCulloch, P. W. M. Blom, A. Salleo, Y. van de Burgt, P. Gkoupidenis, *Sci. Adv.* **2021**, *7*, eabl5068.